Layer-optimized SAR processing with a mobile phase-sensitive radar for detecting the deep englacial stratigraphy of Colle Gnifetti, Switzerland/Italy

Falk M. Oraschewski[1], Inka Koch[1], M. Reza Ershadi[1], Jonathan Hawkins[2], Olaf Eisen[3,4], and Reinhard Drews[1]

[1]University of Tübingen, Department of Geosciences, Tübingen, Germany
[2]Cardiff University, School of Earth and Environmental Sciences, Cardiff, Wales, United Kingdom
[3]Alfred Wegener Institute, Helmholtz Centre for Polar and Marine Research, Bremerhaven, Germany
[4]University of Bremen, Department of Geosciences, Bremen, Germany

Correspondence: Falk M. Oraschewski (falk.oraschewski@uni-tuebingen.de)

Abstract. Radio-echo sounding is a standard technique for imaging the englacial stratigraphy of glaciers and ice sheets. In most cases, internal reflection horizons (IRHs) represent former glacier surfaces and comprise information about past accumulation, ice deformation and allow to link ice core chronologies. IRHs in the lower third of the ice column are often difficult to detect or coherently trace. In the polar ice sheets, progress in IRH detection has been made by using multistatic, phase-coherent radars, enabling synthetic-aperture radar (SAR) processing. However, these radar systems are often not suitable for deployment on mountain glaciers. We present a proof-of-concept study for a lightweight, phase-coherent, and ground-based radar system, based on the phase-sensitive radio echo-sounder (pRES). To improve the detectability of IRHs we additionally adapted a layer-optimized SAR (LO-SAR) processing scheme to this setup. We showcase the system capability at Colle Gnifetti, Switzerland/Italy, and detect significantly deeper and older IRHs compared to previously deployed pulsed radar systems. Continuous IRHs are now apparent down to the base of the glacier. Corresponding reflection mechanisms for this glacier are linked to a stratified acidic impurity which was deposited at a higher rate due to increased industrial activity in the area. Possible improvements of the system are discussed. If successfully implemented, these may provide a new way to map the deep internal structure of Colle Gnifetti and other mountain glaciers more extensively in future deployments.

1 Introduction

Polar mid-latitude glaciers store information about past regional climate change (Wagenbach et al., 2012) and hold natural (Clifford et al., 2019) and anthropogenic (Gabrieli and Barbante, 2014; Sigl et al., 2018a) impurity records that can be extracted by ice coring. Being located in the vicinity of highly industrialized regions (Sigl et al., 2018a), these archives are an important complement to ice core records from the polar ice sheets spanning deep time (EPICA community members, 2004; NEEM community members, 2013). However, the interpretation of these records can be limited by uncertainties in ice core dating (Jenk et al., 2009). Using radar surveys to laterally trace internal reflection horizons (IRHs) between multiple ice core sites, their chronologies can be compared to reduce uncertainties (Eisen et al., 2003; Bohleber, 2011; Licciulli et al., 2020). IRHs

1

represent discontinuities of the dielectric permittivity or conductivity between different layers of ice. Permittivity is controlled through density and crystal-orientation fabric (COF), whereas conductivity is determined through acidity (Fujita et al., 2006). IRHs are isochronous when they are formed by seasonal snow-density variations or impurities that were initially deposited at

25   the surface. Besides supporting the ice core dating, IRHs can be used to infer spatial accumulation patterns (Koch et al., In press.), past ice deformation (Drews, 2015; Koutnik et al., 2016), upstream effects for ice core records (Eisen et al., 2003), and for finding new ice-core sites with an intact stratigraphy (Lilien et al., 2021). In many of these applications the deep and old stratigraphy is of particular interest.

Both on mountain glaciers (Eisen et al., 2003; Konrad et al., 2013) and on polar ice sheets (Drews et al., 2009) the lowest

30   third of the ice column is often difficult to image, for example due to increased radio-wave attenuation, weakening of density contrasts, or buckling and folding of reflection interfaces. For polar ice sheets, the emergence of phase-coherent radars and linked synthetic-aperture radar (SAR) processing have significantly improved the detection of the deep englacial stratigraphy (Hélière et al., 2007; Peters et al., 2007). These heavy and power-intensive systems are pulled by tracked vehicles (Paden, 2006), or mounted on aircrafts (Shi et al., 2010), both of which is not applicable on many mountain glaciers. Instead, smaller,

35   typically incoherent, pulsed ground penetrating radars (GPR) available in a variety of off-the-shelf products are used. Here, we address that a light-weight, low-power, phase-coherent and ground-based system suitable for SAR processing is currently lacking.

SAR processing improves the along-track resolution and suppresses clutter in the radargram by coherently focusing the backscattered power of point targets illuminated across multiple traces (Peters et al., 2005; Kusk and Dall, 2010). Similar

40   to migration, this will collapse along-track hyperbolas from off-nadir reflections, providing improved imaging of, e.g., basal structures. However, in the case of specular reflections from IRHs, the signal quality can also deteriorate during SAR processing due to destructive interference (Holschuh et al., 2014). Castelletti et al. (2019) addressed this shortcoming by introducing a layer optimized SAR (LO-SAR) processing method that corrects for along-track phase shifts of specular reflections before coherent summation. Other approaches for improving the detection of IRHs are based on filtering the IRHs contribution in

45   the azimuth frequency domain of the radargram (Heister and Scheiber, 2018) or on including spatial correlation information into SAR processing (Xu et al., 2022). In addition, most of these algorithms determine the slope of IRHs, which can support the automated tracing of IRHs (MacGregor et al., 2015) and provides an alternative metric for radar data–model comparison (Holschuh et al., 2017).

Here, we showcase a mobile, phase-coherent radar system that is suitable for SAR processing and can be deployed on

50   mountain glaciers. We use the existing phase-sensitive radio echo-sounder (pRES), a light-weight and low-power frequency modulated continuous wave (FMCW) radar operating at 200–400 MHz (Brennan et al., 2014; Nicholls et al., 2015). This technology has been widely used, most prominently in determining basal melt rates beneath ice shelves (Vaňková et al., 2021; Zeising et al., 2022). However, it was originally designed and so far only used for static applications. The feasibility of a mobile deployment has only theoretically been assessed by Kapai et al. (2022) who investigated artifacts that can arise from moving

55   the pRES during data acquisition. Here, we present the first mobile deployment of the pRES in combination with a real-time kinematic (RTK) GPS to achieve the high accuracy in positioning required for SAR processing.
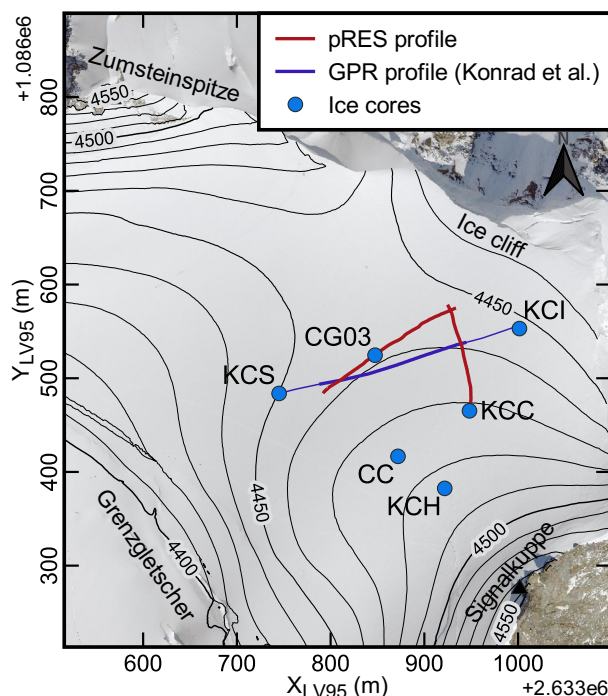
Figure 1. Overview of Colle Gnifetti indicating the location of the collected pRES profiles. The thick part of the GPR profile marks the section that is compared to the across-saddle pRES profile in Fig. 5. Blue dots mark the drill locations of existing ice cores at the time of drilling. Source of orthophoto and elevation model: Federal Office of Topography swisstopo.

We demonstrate that this enables the detection of deep IRHs invisible to previous surveys. In the following we first present the study site (Section 2) and the mobile pRES setup as well as the applied FMCW signal and LO-SAR processing (Section 3). Collected radargrams are compared to GPR data from pulsed systems and to available ice core data to interpret the imaged signatures in the glaciological context (Section 4). Finally, limitations of the mobile pRES are discussed including suggestions for improvements (Section 5).

2 Study site

The Colle Gnifetti is located in the Monte Rosa massif (Swiss–Italian Alps) at an altitude of around 4450 m a.s.l. and forms the upper accumulation zone of Grenzgletscher. It is characterized by low accumulation rates due to wind driven snow erosion (Alean et al., 1983), englacial temperatures below $0°C$ (Hoelzle et al., 2011), and low horizontal flow velocities near the divide (Lüthi and Funk, 2000). In combination, these conditions favor the formation of the longest, still well-preserved, glacial climate record in the European Alps. Several ice cores have been drilled at the site (Fig. 1.), entailing over 1000 years long climate and environmental records (Bohleber et al., 2018). Using radiocarbon dating, Jenk et al. (2009) found indications of more than 10 ka old ice in the CG03 ice core, reaching potentially back into the last glacial period. In the KCC ice core, a discontinuity in
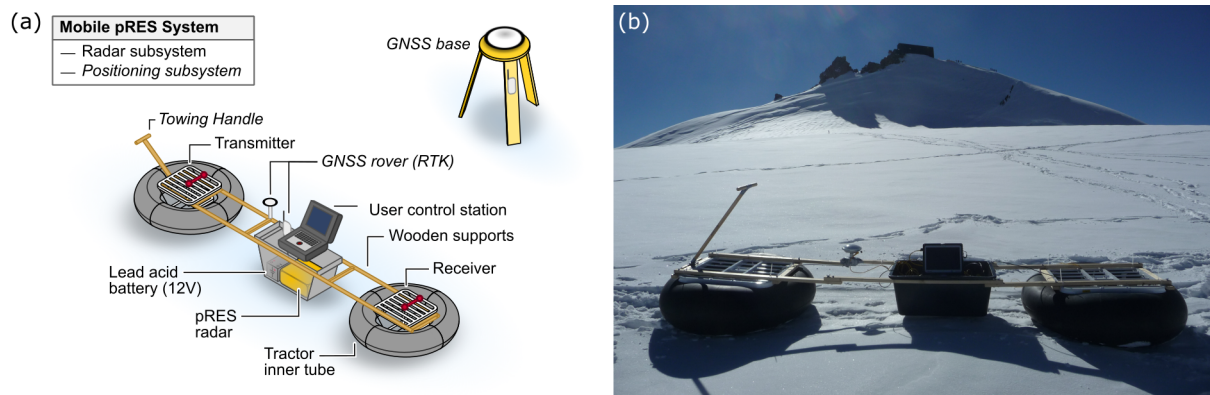
Figure 2. Mobile pRES setup with (a) a schematic of its components and (b) a photograph of the deployment on Colle Gnifetti.

70   the chronology was found by Hoffmann et al. (2018), perhaps because of englacial folding. Radar profiling was conducted to link the chronologies of several ice cores (Eisen et al., 2003; Konrad et al., 2013). However, these studies only detected IRHs in the upper 30–50 % of the glacier with a maximum layer age of 80 years at the time of data acquisition.

3   Methods

In September 2021, we collected 285 m of phase-coherent radar data at Colle Gnifetti using a mobile pRES (Fig. 1; a 166 m
75   long profile across the saddle passing the CG03 ice core, and a second 119 m long profile upstream towards KCC/south). Here, we first describe hardware related aspects for data acquisition with sub-decimeter positioning (Section 3.1). Then, we provide the linked FMCW signal and LO-SAR processing algorithms tailored to that specific measurement setup (Section 3.2). Finally, details about dating IRHs in the collected pRES data (Section 3.3) and about ice core data for assessing the reflectivity decrease at Colle Gnifetti (Section 3.4) are given.

3.1   Data acquisition with the mobile pRES

To mobilize the pRES for profiling, the transmit and receive skeleton antennas were placed in inflated tractor inner tubes with the antennas being separated by 2.7 m and elevated a few centimeters above the snow surface (Fig. 2). The dipole axes of both antennas were oriented perpendicular to the profiling direction, so that the radiation pattern extends further in along-track than in cross-track direction and ground targets are consequently illuminated with more traces in the along-track direction.

85   Due to the long chirp time of the pRES (1 s in standard configuration), data were collected in stop-and-go mode. This suppresses incoherent backscatter, avoids the occurrence of Doppler blurring (Kapai et al., 2022), and reduces system noise which increases when cables move during data acquisition. To make data collection efficient despite this approach, we aimed to minimize the stopping time per point. In the beginning, two chirps were recorded per point/trace from which we only use the one with the lower noise floor. Later, this number was reduced to one chirp. Positioning was controlled by the Trimble
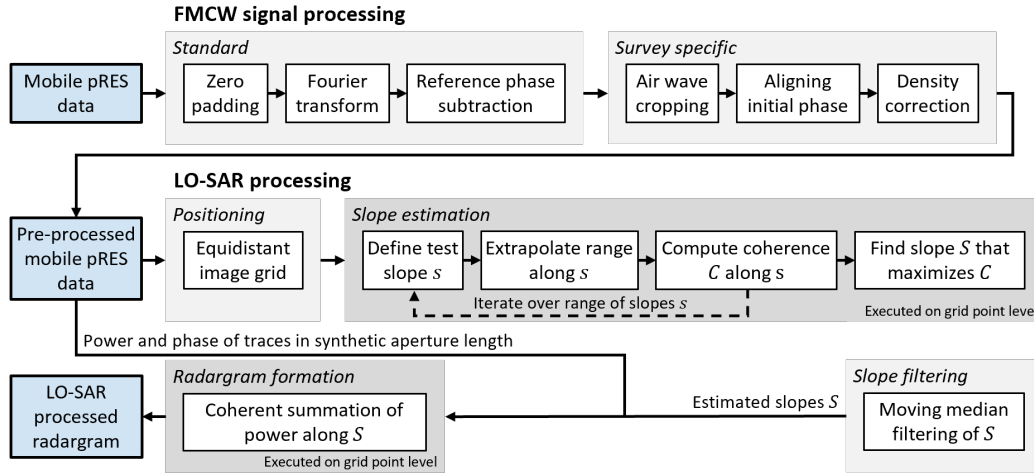
Figure 3. Overview of FMCW signal and LO-SAR processing scheme. Blue boxes represent the radar data at different processing stages. Gray blocks summarize the main processing steps, where a darker gray indicates that these are executed on the grid point level.

R9s GNSS system, operated in RTK mode, with the baseline between the GNSS base station and rover being typically below $200\,\mathrm{m}$. SAR processing only requires relative positions to the base station and we did not post-process the GPS data further. The positioning system was connected to a control station which automatically triggered radar signal acquisition (with the pRES being operated in 'attended mode') once the system was hand-towed by $9\,\mathrm{cm}$ and gave the operator a signal to start/stop towing. With this approach, an average trace spacing of approximately $\Delta d = 13\,\mathrm{cm}$ and a median data acquisition time of $10\,\mathrm{s}$ per trace was achieved, giving a total survey speed of around $3\,\mathrm{h}/100\,\mathrm{m}$.

3.2 Radar processing

This section outlines the processing routine from the raw pRES data to the LO-SAR processed radargram (Fig. 3). We first present the standard FMCW signal processing and summarize survey-specific corrections. This provides the background for estimating the slopes of englacial IRHs from the signal phase for the subsequent LO-SAR processing.

3.2.1 FMCW signal processing

The description of the standard FMCW signal processing and the notation broadly follows Brennan et al. (2014). The pRES transmits a linearly frequency modulated chirp with a center frequency of $f_c = 300\,\mathrm{MHz}$ and a bandwidth $B = 200\,\mathrm{MHz}$ over a chirp time of $T = 1\,\mathrm{s}$. On the hardware side, the reflected signals are mixed with the transmitted signal and subsequently low-pass filtered. This results in the deramped waveform which, by using a fast Fourier transform (FFT), is decomposed into the deramped frequencies

$$f_{\mathrm{d}} = \frac{2B\tilde{R}\sqrt{\varepsilon_{r,\mathrm{ice}}}}{Tc}, \tag{1}$$

which relate to the reflection range $\tilde{R}$ using the speed of light in vacuum c and the real-valued relative permittivity of ice $\varepsilon_{r,\text{ice}} = 3.17$ (Brennan et al., 2014). Note that this formulation does not allow the use of a variable relative permittivity and the reflection range does not consider the lower density of firn (indicated by $\sim$). A density correction will be described below and from here on, the general relative permittivity of firn or ice ε_r is used.

110

The range resolution δ_{R} of FMCW radars is determined by their bandwidth

$$\delta_{\text{R}} = \frac{c}{2B\sqrt{\varepsilon_r}}, \tag{2}$$

giving a resolution of the pRES of $\delta_{\text{R}} = 0.42\,\text{m}$ in ice (Brennan et al., 2014). For each frequency component, or range bin n, the FFT returns the amplitude a_n and phase $\phi_{\text{raw},n}$ in complex form:

115
$$A_{\text{raw},n} = a_n \exp\left(i\phi_{\text{raw},n}\right). \tag{3}$$

Prior to the FFT the deramped waveform is zero-padded, i.e. lengthened with zeros by a padding factor p. This increases the sampling rate of the FFT and reduces the range bin increment to $\Delta R_{\text{bin}} = \delta_R/p$, effectively corresponding to a sinc interpolation of the decomposed amplitude and phase signals. Brennan et al. (2014) suggest using $p \geq 2$ for resolving ambiguities in the phase because, otherwise, the range bins would be separated by more than a full phase cycle (or wavelength, at the center

120 frequency of the pRES). Note, however, that because zero-padding is essentially an interpolation, the intermediate phase cycles cannot be recovered. Nevertheless, the signal phase is typically interpreted relative to an idealized reference phase which, for the center of the n-th range bin, is given by

$$\phi_{\text{ref},n} = n\frac{2\pi f_{\text{c}}}{Bp} - n^2\frac{\pi}{Bp^2 T} \tag{4}$$

(Brennan et al., 2014). The second term is negligible over the operation range of the pRES because $f_{\text{c}} \gg 1/T$, so that

125 $\Delta\phi_{\text{ref,bin}} = 2\pi f_{\text{c}}/(Bp)$. Therefore, $p \geq 2$ ensures that the phase variation of the reference phase between range bins is smaller than 2π. In addition, a high padding improves the representation of the reference phase, which is why we apply a padding factor of $p = 8$ for the subsequent LO-SAR processing.

Subtracting the reference phase ϕ_{ref} from the raw signal results in:

$$A_{\text{cor},n} = a_n \exp\left(i\left(\phi_{\text{raw},n} - \phi_{\text{ref},n}\right)\right)$$
$$= a_n \exp\left(i\phi_{\text{cor},n}\right). \tag{5}$$

130 We denote this phase difference between raw and reference phase as the corrected phase ϕ_{cor} and will exploit that it is constant along sloped IRHs (Fig. 4b) for estimating these slopes during the following LO-SAR processing.

After the standard FMCW signal processing, traces are cropped at the airwave return and shifted to a uniform phase value at zero traveltime. This accounts for spurious π-offsets which appear in some traces for unknown reasons.

Finally, the reflection range $\tilde{R}$, as given in Eq. (1), is density corrected to account for faster wave propagation in firn, which

135 constitutes up to half of the thickness of Colle Gnifetti. This is done by translating $\tilde{R}$ into two-way travel time $\tau = 2\tilde{R}\sqrt{\varepsilon_{r,\text{ice}}}/c$
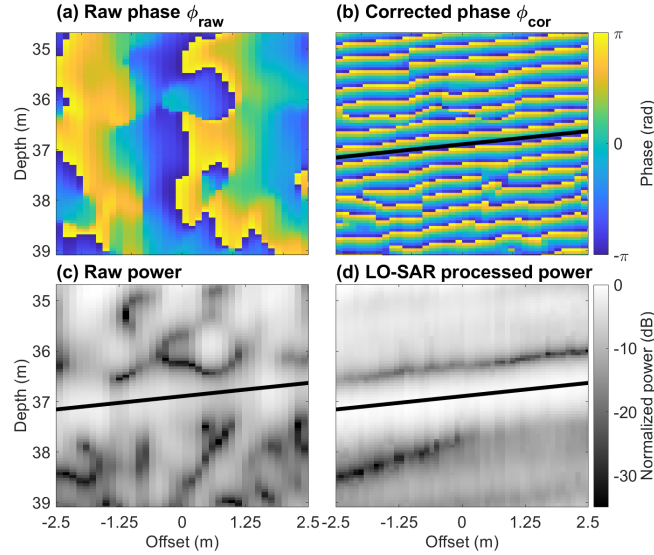
Figure 4. An example segment of the pRES profile over one synthetic aperture length. Phase signal before (a) and after (b) correcting it with a reference signal. Power before (c) and after (d) LO-SAR processing. The slope of the central reflection is indicated by a black line and obtained in (b) by fitting to a coherent section of the reference corrected phase.

and converting them back into corrected ranges R by

$$R(\tau) = \int_0^\tau \frac{c}{2\sqrt{\varepsilon_r}} \, d\tau', \tag{6}$$

using the density data of the KCC ice core (Section 3.4, Freitag et al., 2018) and the relative permittivity given by the Looyenga (1965) mixture model.

3.2.2 Layer Optimized-SAR (LO-SAR) processing

LO-SAR processing optimizes the detection of inclined IRHs by coherently integrating their backscattered power (Fig. 4c) over a fixed aperture length. Our processing is motivated by Castelletti et al. (2019), but differs in the regard that we do not only correct for a phase change before the coherent summation. Instead, we explicitly sum along IRHs after extracting their slopes.

The LO-SAR processed radargram is formed on an equidistant grid where the processed traces are located on a smoothed version of the observed profile line with a spacing of $10\,\mathrm{cm}$. The processing is done grid point by grid point. In the following, we characterize these points (x, z) by their positions x and depths z. For every position, all M observed traces within a distance of $L_{\mathrm{SAR}}/2$ are considered in the radargram formation, with the synthetic aperture length L_{SAR}. Following Castelletti et al. (2019) the Signal-to-Noise ratio (SNR) increases proportional to L_{SAR}. We use $L_{\mathrm{SAR}} = 5\,\mathrm{m}$ which gives a good improvement in radargram quality, while ensuring that IRHs can be assumed to be linearly sloped over the full synthetic aperture length.

First, knowledge of the local slopes S at all grid points is required. In theory, these can be inferred from the unwrapped along-track phase gradient $\Delta\phi_{\text{trace}}$ between the neighboring observed traces which quantifies the local change in reflection depth ΔR_{IRH} (MacGregor et al., 2015), as given by the general relation between phase and range differences:

$$\Delta R = \frac{\lambda_{\text{c}}\Delta\phi}{4\pi}, \tag{7}$$

155   where $\lambda_{\text{c}} = c/\left(\sqrt{\varepsilon_r}f_{\text{c}}\right)$ is the wavelength that corresponds to the center frequency. The local englacial slope is then:

$$\begin{aligned} S(x,z) &= \arctan\left(\frac{-\Delta R_{\text{IRH}}(x,z)}{\Delta d(x)}\right) \\ &= \arctan\left(\frac{-\lambda_{\text{c}}\Delta\phi_{\text{trace}}(x,z)}{4\pi\Delta d(x)}\right). \end{aligned} \tag{8}$$

However, this method directly translates uncertainties in the phase, e.g. due to occasional faulty traces and phase jumps at the transition between IRHs, into uncertainties in the slope, which limits the accuracy of slope detection in this way in our data.

We circumvent this problem by not only considering the phase-gradient, but also the coherence of the phase during slope

160   estimation. For this we exploit that the corrected phase is constant along IRHs (Fig. 4b). In practice, we iterate for each grid point over a range of slopes s (from $-30°$ to $30°$ in steps of $0.2°$) to compute the coherence of the corrected phase along a line with length L_{SAR} and slope s, centered around (x,z). Its depth at the M observed traces within the synthetic aperture length is given by

$$R_m(x,z,s) = z + (x_m - x)\tan(s), \tag{9}$$

165   with the position of the observed traces x_m. The corrected signal of the m-th trace on that line $A_{\text{cor},m}(x,z,s)$ is then obtained by the weighting the values in the adjacent range bins above and below $R_m(x,z,s)$. Using these, we define the local phase coherence at (x,z) along slope s:

$$\begin{aligned} C(x,z,s) &= \left|\frac{1}{M}\sum_{m=1}^{M}\frac{A_{\text{cor},m}(x,z,s)}{|A_{\text{cor},m}(x,z,s)|}\right| \\ &= \left|\frac{1}{M}\sum_{m=1}^{M}\exp\left(i\phi_{\text{cor},m}(x,z,s)\right)\right|. \end{aligned} \tag{10}$$

The slope along which the coherence is largest then gives the local englacial slope S:

170   $$S(x,z) = \arg\max_{s}\left(C(x,z,s)\right). \tag{11}$$

This approach gives a more consistent slope estimate than the direct computation using Eq. (8), but still may provide erroneously high values at the interface between different IRHs. To remove these, we apply a moving median filter to the slope field using a filtering window of $2\,\text{m}\times 2\,\text{m}$.

Finally, the LO-SAR processed radar image is obtained by coherent summation of A_{cor} along the determined slope S:

175   $$A_{\text{LO-SAR}}(x,z) = \left|\frac{1}{M}\sum_{m=1}^{M}A_{\text{cor},m}(x,z,S(x,z))\right| \tag{12}$$

This defines the LO-SAR processed amplitude $A_{\text{LO-SAR}}$ at each grid point (Fig. 4d).

3.3 Dating of internal reflection horizons

In the LO-SAR processed radargram, we picked and dated two IRHs and compare these with the deepest IRH from previous studies (Fig. 5). The age estimate of the newly picked IRHs is obtained from the model chronology of Jenk et al. (2009) for the CG03 ice core which is located on the profile (Fig. 6). For this, range values were converted into units of m w.e. to match their formulation of the age–depth model. Uncertainties arise both, from dating of the ice core and from estimating the reflection range. To obtain ice core dating uncertainties, we computed the confidence limits of the age–depth model at both IRHs giving an uncertainty of $5\,\mathrm{a}$ in the upper and $27\,\mathrm{a}$ in the lower picked IRH. The range uncertainty is again attributed to two factors: To the inherent uncertainty associated with the width of radar reflections and to the uncertainty in the firn correction applied to the radar data. The latter was estimated as the given range difference between using the KCC or CG03 firn density data (Section 3.4) for density correction. In combination, both factors give a range uncertainty on the order of $1\,\mathrm{m}$ (Fig. 6). The full dating uncertainty of both IRHs were computed by error propagation of all three contributing factors.

3.4 Ice core data for radar signal interpretation

This study considers ice core data from the KCC ice core (Freitag et al., 2018), drilled in 2013, and the CG03 ice core (Sigl et al., 2018b), drilled in 2003 (Fig. 1). The latter was measured in the upper $57.2\,\mathrm{m}$ and extended at the top by the shallow core CG15, drilled at the same location in 2015 (Sigl et al., 2018b). Firn density data of CG03 were obtained by weighting ice core segments of $\sim 70\,\mathrm{cm}$ length (M. Sigl, personal communication), and for KCC by X-ray computer tomography in $\sim 2\,\mathrm{mm}$ resolution (Freitag et al., 2018). For CG03/CG15 we estimate the acidity by computing the ion balance between the concentrations of Calcium, Sodium, Ammonium, Nitrate and Sulfate (Ca^{2+}, Na^+, NH_4^+, NO_3^- and SO_4^{2-}) measured in the cores. In addition, we compute the ion balance without Ca^{2+} to exclude its dominating contribution for the further interpretation. For comparison with the radar signal, the acidity records with a resolution of $\sim 3\,\mathrm{cm}$ are smoothed by a Gaussian filter with a width of $48\,\mathrm{cm}$, which is approximately the mean resolution of the pRES in firn.

4 Results

4.1 Radar profiling at Colle Gnifetti

The transect from KCS to KCI (Fig. 1) from Konrad et al. (2013) is a representative example for numerous conventional pulsed GPR surveys conducted at Colle Gnifetti. These have mapped IRHs in the upper 30–50 % of the ice column, whereas the deeper ice appeared basically echo-free (Fig. 5a). The deepest IRH detectable in this radargram had an age of $78 \pm 12\,\mathrm{a}$ at the time of recording, which corresponds to the year 1930 CE. Note that Konrad et al. (2013) did not assign an age value to this IRH, and we repeated their approach for younger IRHs of averaging the KCS and KCI ages. In these data, the ice–bedrock interface is inconsistently detected and in some cases cannot be identified (e.g., Fig 3.8 in Bohleber, 2011).

Our pRES profile collected across the saddle intersects with the GPR profile by Konrad et al. (2013). Already in the raw data, ice and bedrock are distinguishable and deeper IRHs are visible prior to the LO-SAR processing (Fig. 5c). However, these
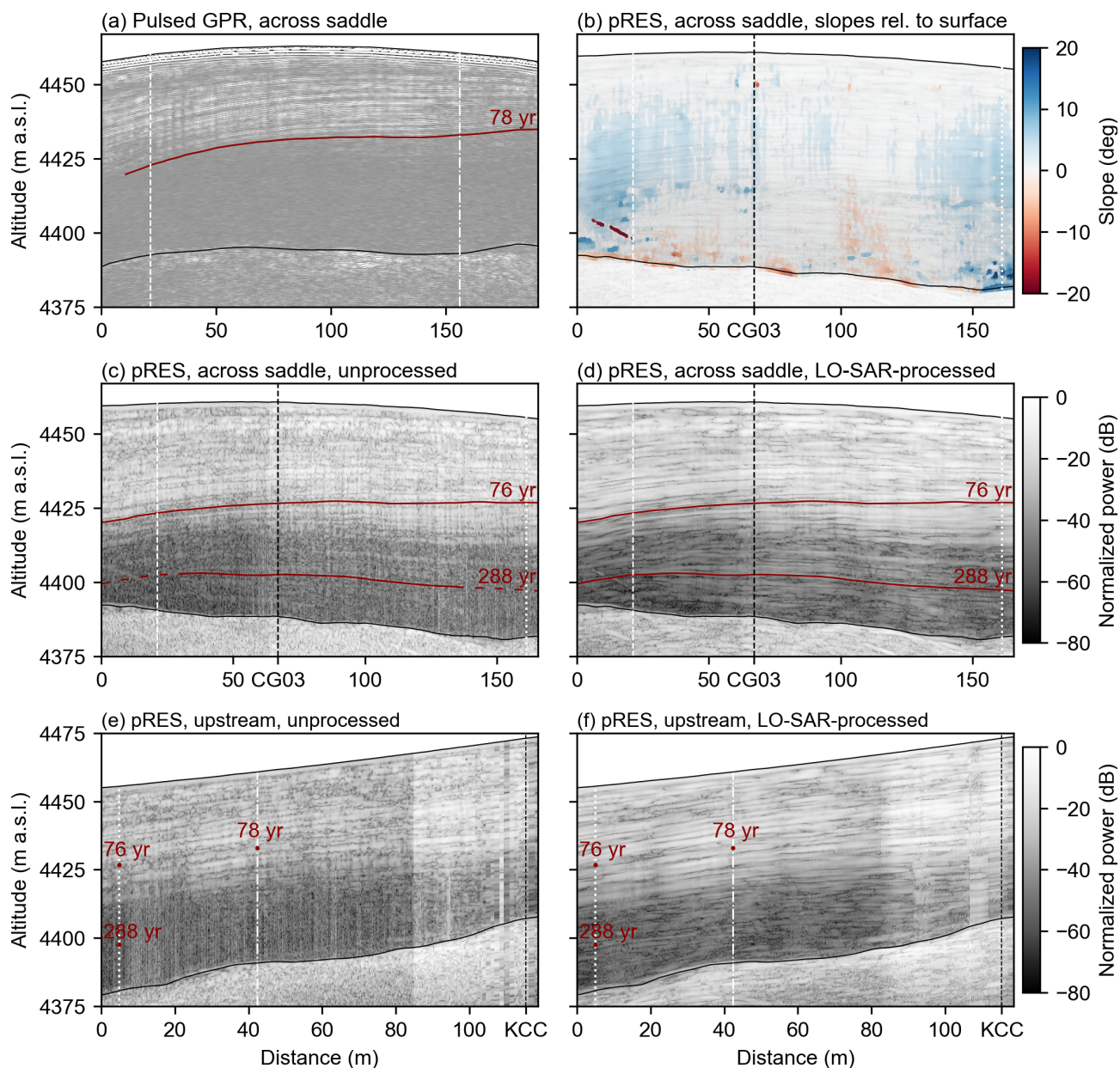
Figure 5. Comparison of radargrams (a–d) across Colle Gnifetti and (e–f) upstream towards KCC. (a) Radar data of a pulsed GPR (Konrad et al., 2013); (b) IRH slopes relative to the surface derived from the corrected phase of the mobile pRES data; (c, e) mobile pRES data before and (d, f) after LO-SAR processing. Red lines mark picked IRHs. In the upstream profile (e–f), picking of deep IRHs is prevented by lower data quality due to technical problems and red dots only indicate the IRHs picked in the other profiles. The intersection points between the three profiles are marked by differently interrupted white lines. The CG03 and KCC ice core locations are marked by black dashed lines.
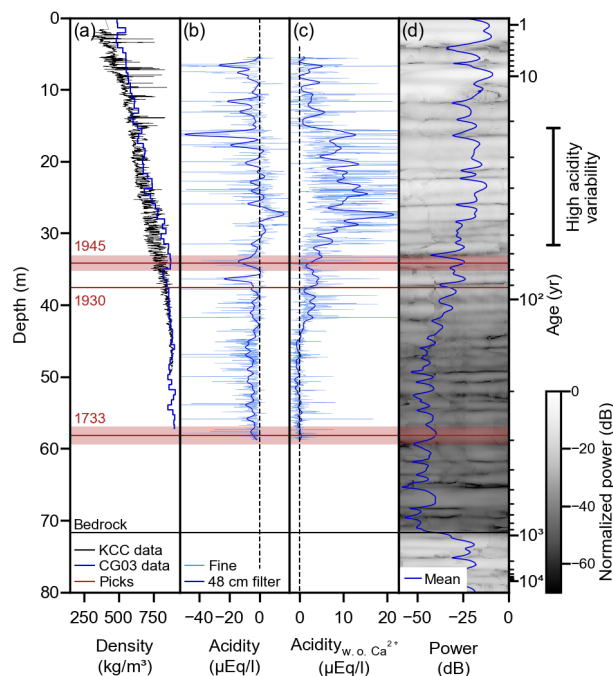
Figure 6. Comparison of mobile pRES power with data from the CG03/CG15 (Sigl et al., 2018b) and KCC (Freitag et al., 2018) ice cores. (a) Firn density; (b) Acidity estimated by ion balance in fine resolution (2 cm) and after applying a 48 cm Gaussian filter; (c) as (b), after excluding Ca^{2+} from the ion balance; (d) Radar section (2 m) around CG03 and its mean power. Red lines mark picked IRHs, with error bands of the 1945- and 1733-horizons illustrating the uncertainty in the range estimate. Ages are computed using the age–depth model of Jenk et al. (2009).

IRHs are yet difficult to trace in parts due to persistent speckle noise. Moreover, IRH quality deteriorates in the flanks of the saddle where they are more inclined. This inclination relative to the surface is quantified during the LO-SAR processing and

210 attains values of about 10° at both ends (Fig. 5b). The LO-SAR processed data exhibits deep IRHs which were not apparent in the previous surveys (Fig. 5d). In the profile collected upstream towards KCC (Fig. 5e–f), LO-SAR processing also reveals the presence of deep specular reflections. However, because of poorer data quality, our data does not show IRHs that are continuous over the whole upstream transect.

We traced two IRHs in the pRES radargram acquired across the saddle and linked them to the chronology of the CG03 ice

215 core (Jenk et al., 2009). The first IRH matches the 78 a-horizon in the pulsed GPR data with respect to depth at the intersection between both profiles. It was independently dated to an age of 76 ± 7 a or the year 1945 CE. The second IRH with an age of 288 ± 35 a (i.e. the year 1733 CE) marks the deepest reflection that is continuously traceable in the LO-SAR processed radargram. But even at greater depths IRHs are visible in parts.

11

4.2 Comparison to ice core data

220 Similar to previous GPR surveys from Colle Gnifetti, the LO-SAR processed radar data shows a distinct contrast in radio-backscatter between the upper and the lower part of the ice column. In the following, we investigate if available ice-core data of firn density and acidity provides evidence as to why this is the case. Variations of both properties, together with COF, are potential reflection mechanisms that can form IRHs.

Both at CG03 and KCC, firn compaction occurs in the upper $\sim 40\,\mathrm{m}$ (Fig. 6a). Most variability in density is observed in the
225 top $15\,\mathrm{m}$, where melt layers are identified in the high-resolution record of the KCC core (Freitag et al., 2018).

Acidity is approximated by the ion balance between the concentrations of Ca^{2+}, Na^+, NH_4^+, NO_3^- and SO_4^{2-} at CG03 (Fig. 6b). The balance is dominated by alkaline peaks, which are caused by Ca^{2+} and represent major Saharan dust deposition events (e.g., in $1936\,\mathrm{CE}/36.5\,\mathrm{m}$ depth, Sigl et al., 2018a). By excluding Ca^{2+} from the ion balance, a trend from alkaline conditions in the pre-industrial to more acidic conditions during the 20th century, which initiates at a depth of $45\,\mathrm{m}$, becomes
230 apparent (Fig. 6c). These more acidic conditions are accompanied by a generally higher variability of the acidity itself, which is most pronounced in the fine resolution record between 15–$32\,\mathrm{m}$ depth.

The power profile of the recorded pRES data at CG03 shows a highly reflective regime in the top $36\,\mathrm{m}$, where reflections mostly attain values above $-25\,\mathrm{dB}$, and a low reflective regime below $45\,\mathrm{m}$ depth, where the returned power rarely exceeds $-40\,\mathrm{dB}$. In between these two regimes, the power level drops abruptly over less than $10\,\mathrm{m}$. The bedrock reflections have a
235 normalized power above $-25\,\mathrm{dB}$, again.

5 Discussion

5.1 Feasibility assessment

Our proof-of-concept study demonstrates the capability of the pRES to expand the range over which englacial stratigraphy can be detected, which is a clear improvement over previous surveys that used pulsed GPRs. However, it comes at the cost of
240 significantly slower data acquisition (Section 3.1), which takes several hours as opposed to several tens of minutes with pulsed GPRs. This results from the required high spatial sampling rate and the long chirp time of $1\,\mathrm{s}$ of the pRES (which is not a limiting factor for its intended stationary surveys). In combination, these factors make data collection in stop-and-go mode necessary.

This raises the question whether pulsed GPRs can achieve similar detection ranges when being operated in stop-and-go
245 mode and by applying high stacking rates, equivalent to the $1\,\mathrm{s}$ chirp time, to suppress incoherent backscatter. Although we cannot answer this question directly, we note that even if these GPRs can achieve a SNR comparative to the unprocessed pRES data (Fig. 5c), they will not be able to match the SNR potentially achievable by phase-based radar processing Fig. 5d).

Therefore, we suggest that the objective of further research should not be a more painstaking data collection using pulsed GPRs but rather aim at accelerating the profiling capabilities of FMCW radars, because the laborious data acquisition is the key

250 limitation for mobile operation of the pRES, restricting the current applicability of the system to targeted small scale surveys. In the following, we discuss how to accelerate data acquisition in future deployments.

The required spatial sampling rate for LO-SAR processing is set by the fact that reflections need to be traceable (Schroeder et al., 2019). The slope of IRHs can only be derived from the phase when it changes by less than π between neighboring traces, otherwise, spatial aliasing occurs. Thus, following Eq. (8) the minimal required trace spacing to resolve IRHs with a slope s is

255 given by

$$\Delta d < \frac{\lambda_\mathrm{c}}{4\tan(s)}. \tag{13}$$

In snow and firn-covered glacial ice, GPR can only record IRHs with a maximum slope of approximately $45°$ (Holschuh et al., 2014). Accordingly, a trace spacing of less than $14\,\mathrm{cm}$ is required to record IRHs of such slopes. This also suffices the threshold of $\Delta d < \lambda_\mathrm{c}/2$ to avoid the occurrence of grating lobes when imaging (basal) point reflectors (Kapai et al., 2022). A coarser

260 trace spacing can be used, when only IRHs with a lower inclination are expected at the study site.

Nevertheless, if the requirement for stop-and-go measurements can be loosened, a high spatial sampling rate is less of a problem. This can either be achieved by reducing the potential noise due to movement of the pRES during chirp acquisition or by reducing the chirp time. Electrical noise by cable motion can be reduced by using phase-stable cables in future deployments (Hati et al., 2009). However, increased noise by averaging signals of multiple reflections and the occurrence of Doppler blurring

265 and grating lobes (Kapai et al., 2022) can only be avoided when moving with very low speeds. Fortunately, these problems are not of physical, but of technical nature and can again be avoided by reducing the chirp time.

The chirp time T of a FMCW radar determines the deramped frequency at a given range (Eq. 1). The pRES was designed to monitor up to $2\,\mathrm{km}$ thick polar ice, which for a chirp time of $1\,\mathrm{s}$ gives a maximum deramped frequency of $4.7\,\mathrm{kHz}$. The build-in data logger of the pRES with a sampling rate of $40\,\mathrm{kHz}$ was chosen accordingly (Brennan et al., 2014) and sets the

270 lower limit of the chirp time. However, for deployment of the pRES on less thick ice this means that the chirp time of the pRES can be reduced. For example, for surveying less than $200\,\mathrm{m}$ thick ice, as we do in this study, a $90\,\%$ shorter chirp time could safely be selected without exceeding the sampling rate of the data logger. Even faster chirp times in the μs-range are desirable, but require a redesign of the hardware.

A second limitation of the pRES lies in its range resolution, which is 2.5 times higher, i.e. worse, compared to the previ-

275 ously used $250\,\mathrm{MHz}$ pulsed GPRs. The latter have a theoretical vertical resolution of $0.17\,\mathrm{m}$ as given by $\delta_{R,\mathrm{GPR}} = \lambda_\mathrm{GPR}/4 = c/(4\sqrt{\varepsilon_r}f_\mathrm{GPR})$. The resolution of FMCW radars is determined by their bandwidth, following Eq. (2): $\delta_{R,\mathrm{FMCW}} = c/(2\sqrt{\varepsilon_r}B_\mathrm{FMCW})$. For the pRES with $B = 200\,\mathrm{MHz}$ this gives a vertical resolution of only $0.43\,\mathrm{m}$. $250\,\mathrm{MHz}$ pulsed GPRs are consequently better at detecting shallower IRHs. To achieve a comparable resolution with a FMCW system, a bandwidth of $500\,\mathrm{MHz}$ is required.

5.2 Slope estimation

280 The presented LO-SAR processing is also computationally expensive, primarily because of the slope estimation algorithm. For short profiles, this is less of a problem (in the examples provided here the compute time was 12 hours on a normal performing Desktop computer), but it might be a restriction for more extensive mobile pRES surveys in the future.

Direct computation of englacial slopes from horizontal gradients of the phase as introduced by MacGregor et al. (2015) is significantly faster. But it also gives a less accurate estimate, because it operates on a point-by-point (i.e. zero-dimensional)
285 base and directly translates noise in the phase into noise in the slopes. For this reason, we derive the slopes of IRHs by matching slope lines to the corrected phase. As this is a one-dimensional approach we combine the information from adjacent traces and get a more accurate slope estimate.

A third method to derive englacial slopes is based on the Radon transform, which operates on a two-dimensional window and computes line integrals over a range of possible slopes and intercepts (Holschuh et al., 2017). Similar to our approach, the
290 Radon transform is computed for every grid point and the correct slope is selected as the one which gives the most coherent stack. Although this is even more computationally expensive, it does not improve the slope estimate further compared to our approach. This can be attributed to the fact that we essentially perform a one-dimensional Radon transform, which only considers an intercept of zero. This is possible because we obtain the coherence along the line integrals from the coherence of the phase and not from the coherence of structural patterns, as the two-dimensional Radon transform does.

295 It should be noted that our use of the corrected phase in fact contradicts with its intended purpose of indicating a fine range offsets for each range bin, as suggested by Brennan et al. (2014). They introduced it as the phase differences between the raw and the reference phase, which following Eq. (7) would translate into range offsets. However, this approach relies on the assumption that the raw phase values in each range bin are independent. This would be expressed by a clear inter-bin variability of the raw phase, which cannot be observed (Fig. 4a). Instead, strong reflections spread out over several range bins,
300 across which the raw phase tends to be stable and distinct jumps of the raw phase only occur at the transition between different reflections.

Under the assumption that the raw phase is constant in the vertical, it becomes clear why the corrected phase is constant along IRHs. The information about IRH slopes is entailed in the along-track gradient of the phase. When the phase of an IRH has increased by $\phi_{\mathrm{ref,bin}}$ in the horizontal, it will have moved down by one range bin. But as the raw phase of each reflection
305 is approximately constant in the vertical, by subtracting exactly $\phi_{\mathrm{ref,bin}}$ from the next range bin during phase correction, the value of the corrected phase at for example the center of an IRH will remain constant.

Our final slope estimate shows some noticeable vertical bands (Fig. 5b). These are most likely no englacial signals, but are caused by antenna tilt due to small-scale surface undulations. However, the slopes are only an intermediate product in our LO-SAR processing routine. In the subsequent coherent summation along IRHs, we specifically aim to follow IRHs, also across
310 such undulations. For this reason, these artifacts are of no concern in our study, but might be relevant in other applications of the slope estimate.

5.3 Detection of deep IRHs

The data collected with the mobile pRES reproduces and expands the results of previous surveys. We identified an IRH with an age of 76 ± 7 a at the time of recording that with respect to depth matches the deepest detectable horizon (78 ± 12 a) in the
315 survey by Konrad et al. (2013). By observing several deeper IRHs in our data, we demonstrate that LO-SAR processed mobile pRES data can be used to inter-compare ice-core chronologies at Colle Gnifetti for larger depth and age ranges than what was

possible before. We shifted this limit to at least 288 ± 35 a. This can be attributed to a combination of accurate data acquisition and system hardware leading to a high SNR, and enhancement of signal coherence by the applied LO-SAR processing.

The system can in principle illuminate the englacial structure over the whole ice column. The data indicate the presence of a
320 layered stratigraphy down to bedrock, which implies that older IRHs are potentially also preserved and might be traceable by further improvements in the processing and suppression of uncertainty sources. In particular, our data acquisition was affected by technical problems, which might have arisen from overexerting the data writing capacity of the pRES after collecting > 1000 individual traces in a single folder. Thereby, various later recorded traces were lost or showed an enhanced noise level. This diminished the data quality of the second part of the pRES profile collected upstream towards KCC (Fig. 5e–f). In addition, this
325 part might have been affected by a less stable positioning of the mobile pRES system at each point due to the increased surface slope. As a consequence, deep IRHs in the upstream profile are disturbed and not continuously traceable, which prevents linking the CG03 and KCC ice cores with our data.

A caveat in interpreting deep IRHs and linking them to ice cores, lies in their associated depth-uncertainty and in potential interference by the bedrock reflector. At the location of the CG03 ice core, the ice–bed interface appears in our radar data at a
330 range of 72 m (Fig. 6d), whereas the ice core itself has a length of 80.2 m (Jenk et al., 2009). This mismatch can be attributed to a potentially non-straight orientation of the borehole, and steep gradients in the bedrock topography of Colle Gnifetti, which affect the apparent position of the bedrock reflector in the radar data (Eisen et al., 2003; Bohleber, 2011). Following (Moran et al., 2000), three-dimensional array processing and correspondingly dense profile grids are needed at steeply sloping topography to accurately measure the bedrock reflector depth. With only two-dimensional profiling, an accuracy on the order
335 of 10 m is to be expected. Moreover, unlike traditional SAR processing methods, the LO-SAR processing does not provide a range migration, but merely aims at improving the SNR of the radargram.

Because of the complex basal topography, it is moreover possible that near-basal IRHs are masked by the 15 dB stronger cross-track bedrock reflections, if these IRHs are not similarly recorded from cross-track angles. Expanding our setup with a multi-channel cross-track antenna array (Castelletti et al., 2017; Holschuh et al., 2020; Scanlan et al., 2020) would allow to
340 decipher the true origin of the near-basal IRH and bed returns and help in locating, separating and interpreting their signatures.

5.4 Origin of the reduced radar backscatter in the lower half of the ice column

By observing deep IRHs that are undisturbed and nearly flat, it can be excluded that their apparent absence in earlier surveys was caused by buckling or folding of reflectors, or a complete degradation of dielectric contrasts. Direct comparison of the reflected power of observable IRHs with ice core records of density and acidity allows us to assess the dominant reflection
345 mechanisms at Colle Gnifetti and the origin of the drop in backscattered power. Strong density variations due to melt layers are only present in the top 15 m and are likely causing near-surface IRHs. Further down, especially below 35 m depth, density contrasts are significantly weaker, show no correlation with the backscattered power, and, therefore, do not control the reflection mechanism.

Accordingly, deep IRHs are caused by impurities, determining the acidity and perhaps even promote changes in the COF.
350 As noted by Eisen et al. (2003), the deep ice is more alkaline due to smaller emissions in the past, reducing its conductivity.

However, it is not the general acidity level which induces reflections, but variations of it. By computing the ion balance between Ca^{2+}, Na^+, NH_4^+, NO_3^- and SO_4^{2-}, measured in the CG03 ice core (Sigl et al., 2018a), we obtained a high-resolution estimate of the acidity. It is dominated by prominent peaks in Ca^{2+} (Fig. 6b), which is a proxy for Saharan Dust (Sigl et al., 2018a). An example is the $1936\,\mathrm{CE}$ peak in $36\,\mathrm{m}$ depth which appears as a strong IRH in the radar data (Fig. 6d) that marks the onset of the power drop. Major Saharan dust deposition events occur on a decadal timescales, with an increasing frequency only in the last 4 decades, attributed to increasing drought conditions in northern Africa (Sigl et al., 2018a). In combination with other natural deposition, for example due to volcanic activity and forest fires, this sets the natural background for acidity variations at Colle Gnifetti.

By excluding Ca^{2+} from the ion balance, the impact of anthropogenic pollution is highlighted (Fig. 6c). In particular, the deposition of NH_4^+, NO_3^- and SO_4^{2-} is largely controlled by anthropogenic activity (Preunkert et al., 2003; Schwikowski et al., 1999) and correlates with other industrial emissions (e.g., refractory black carbon, Sigl et al., 2018a). Starting in $1875\,\mathrm{CE}$, which corresponds to $45\,\mathrm{m}$ depth at CG03 and the onset of industrialization in Western Europe (Sigl et al., 2018a), higher concentrations of these pollutants can be observed. These do not only shift the ice chemistry to more acidic conditions, but in particular correspond to an accelerated rate of impurity deposition events, most notable between $15\,\mathrm{m}$ and $32\,\mathrm{m}$ depth. This high acidity variability strongly correlates with the strength of backscattered power, because acidity contrast fosters IRH formation. Accordingly, the shift between a high- and a low-reflective regime at Colle Gnifetti, is caused by a shift from deposition of natural impurities at a low rate to anthropogenic pollution at a high rate.

In addition to altering the acidity, impurity layers might cause localized changes of the COF which additionally modulate the reflectivity at Colle Gnifetti. In a seismic profile collected across the KCI ice core, Diez et al. (2013) detected an englacial reflection $5\,\mathrm{m}$ above the bedrock, which they attributed to changes in the crystal orientation. In our data, this reflection might correspond to the comparatively strong IRH at $67\,\mathrm{m}$ depth.

6 Conclusions

We presented a proof-of-concept study for coherent radar profiling with a mobile pRES that is positioned using a RTK GPS. In combination with LO-SAR processing, this enables the detection of the deep englacial stratigraphy of Colle Gnifetti. This is a clear step forward compared to previous GPR surveys where IRHs could only be detected in the upper 30–50 % of the ice column. Our study demonstrates the possibility to extensively map the deep structure of Colle Gnifetti in future deployments. Such a targeted survey could connect all previous ice core locations to inter-compare their chronologies and address open questions in the understanding of existing ice core records, such as the origin of the discontinuity in the chronology of the KCC ice core. Moreover, it can aid the selection of future ice core drilling sites, for example to find the deepest, and potentially oldest, preserved stratigraphically intact ice in the saddle, and therefore in the European Alps. As the applicability of our approach is however limited by time-intensive data acquisition due to the long chirp time of the pRES, we have provided suggestions on how to accelerate it in future deployments. By comparison to ice core data, we in addition identified that the reflection pattern at Colle Gnifetti is controlled by acidity variations due to the deposition of impurities. The presence of a highly reflective regime

385 in the upper part of the glacier (which was detectable in earlier surveys) compared to a less reflective regime in the bottom part (which previously appeared echo-free), is caused by acidic impurity layers that are deposited at a high rate since the onset of industrialization. Only comparatively modest technical improvements are required to deploy this phase-coherent radar in other geoscientific settings, opening up new avenues for scientific applications based on FMCW radars.

Code and data availability. Publication of the raw and processed pRES radar data and the LO-SAR processing code are in preparation.

Author contributions. FMO led the data acquisition, analysis and writing of the paper. FMO, RD and OE designed the study outline and
390 FMO, RD, IK and MRE conducted the data acquisition. JH supported the analysis of the data and designed Fig. 2a. All authors contributed to the writing of the final paper.

Competing interests. RD and OE are members of the editorial board of The Cryosphere. The authors have no other competing interests to declare.

References

Alean, J., Haeberli, W., and Schädler, B.: Snow Accumulation, Firn Temperature and Solar Radiation in the Area of the Colle Gnifetti Core
400   Drilling Site (Monte Rosa, Swiss Alps): Distribution Patterns and Interrelationships, Zeitschrift für Gletscherkunde und Glazialgeologie,
19, 131–147, http://hdl.handle.net/10013/epic.40215.d001, 1983.

Bohleber, P.: Ground-Penetrating Radar Assisted Ice Core Research: The Challenge of Alpine Glaciers and Dielectric Ice Properties, Ph.D.
thesis, Heidelberg University, https://doi.org/10.11588/heidok.00012800, 2011.

Bohleber, P., Erhardt, T., Spaulding, N., Hoffmann, H., Fischer, H., and Mayewski, P.: Temperature and Mineral Dust Variability Recorded in
405   Two Low-Accumulation Alpine Ice Cores over the Last Millennium, Clim. Past, 14, 21–37, https://doi.org/10.5194/cp-14-21-2018, 2018.

Brennan, P. V., Lok, L. B., Nicholls, K., and Corr, H.: Phase-sensitive FMCW Radar System for High-precision Antarctic Ice Shelf Profile
Monitoring, IET Radar, Sonar & Navigation, 8, 776–786, https://doi.org/10.1049/iet-rsn.2013.0053, 2014.

Castelletti, D., Schroeder, D. M., Hensley, S., Grima, C., Ng, G., Young, D., Gim, Y., Bruzzone, L., Moussessian, A., and Blankenship,
D. D.: An Interferometric Approach to Cross-Track Clutter Detection in Two-Channel VHF Radar Sounders, IEEE Trans. Geosci. Remote
410   Sensing, 55, 6128–6140, https://doi.org/10.1109/TGRS.2017.2721433, 2017.

Castelletti, D., Schroeder, D. M., Mantelli, E., and Hilger, A.: Layer Optimized SAR Processing and Slope Estimation in Radar Sounder
Data, J. Glaciol., 65, 983–988, https://doi.org/10.1017/jog.2019.72, 2019.

Clifford, H. M., Spaulding, N. E., Kurbatov, A. V., More, A., Korotkikh, E. V., Sneed, S. B., Handley, M., Maasch, K. A., Loveluck, C. P.,
Chaplin, J., McCormick, M., and Mayewski, P. A.: A 2000 Year Saharan Dust Event Proxy Record from an Ice Core in the European
415   Alps, JGR Atmospheres, 124, 12 882–12 900, https://doi.org/10.1029/2019JD030725, 2019.

Diez, A., Eisen, O., Hofstede, C., Bohleber, P., and Polom, U.: Joint Interpretation of Explosive and Vibroseismic Surveys on Cold Firn for
the Investigation of Ice Properties, Ann. Glaciol., 54, 201–210, https://doi.org/10.3189/2013AoG64A200, 2013.

Drews, R.: Evolution of Ice-Shelf Channels in Antarctic Ice Shelves, The Cryosphere, 9, 1169–1181, https://doi.org/10.5194/tc-9-1169-2015,
2015.

420 Drews, R., Eisen, O., Weikusat, I., Kipfstuhl, S., Lambrecht, A., Steinhage, D., Wilhelms, F., and Miller, H.: Layer Disturbances and the
Radio-Echo Free Zone in Ice Sheets, The Cryosphere, 3, 195–203, https://doi.org/10.5194/tc-3-195-2009, 2009.

Eisen, O., Nixdorf, U., Keck, L., and Wagenbach, D.: Alpine Ice Cores and Ground Penetrating Radar: Combined Investigations
for Glaciological and Climatic Interpretations of a Cold Alpine Ice Body, Tellus B, 55, 1007–1017, https://doi.org/10.1034/j.1600-
0889.2003.00080.x, 2003.

425 EPICA community members: Eight Glacial Cycles from an Antarctic Ice Core, Nature, 429, 623–628, https://doi.org/10.1038/nature02599,
2004.

Freitag, J., Kerch, J., Hoffmann, H., Spaulding, N., and Bohleber, P.: XCT Density from the Alpine Ice Core KCC (2013),
https://doi.org/10.1594/PANGAEA.887691, 2018.

Fujita, S., Maeno, H., and Matsuoka, K.: Radio-Wave Depolarization and Scattering within Ice Sheets: A Matrix-Based Model to Link Radar
430   and Ice-Core Measurements and Its Application, J. Glaciol., 52, 407–424, https://doi.org/10.3189/172756506781828548, 2006.

Gabrieli, J. and Barbante, C.: The Alps in the Age of the Anthropocene: The Impact of Human Activities on the Cryosphere Recorded in the
Colle Gnifetti Glacier, Rend. Fis. Acc. Lincei, 25, 71–83, https://doi.org/10.1007/s12210-014-0292-2, 2014.

Hati, A., Nelson, C. W., and Howe, D. A.: Vibration-Induced PM and AM Noise in Microwave Components, IEEE Trans. Ultrason., Ferro-
elect., Freq. Contr., 56, 2050–2059, https://doi.org/10.1109/TUFFC.2009.1288, 2009.

435   Heister, A. and Scheiber, R.: Coherent Large Beamwidth Processing of Radio-Echo Sounding Data, The Cryosphere, 12, 2969–2979, https://doi.org/10.5194/tc-12-2969-2018, 2018.

Hélière, F., Lin, C.-C., Corr, H., and Vaughan, D.: Radio Echo Sounding of Pine Island Glacier, West Antarctica: Aperture Synthesis Processing and Analysis of Feasibility from Space, IEEE Trans. Geosci. Remote Sensing, 45, 2573–2582, https://doi.org/10.1109/TGRS.2007.897433, 2007.

440   Hoelzle, M., Darms, G., Lüthi, M. P., and Suter, S.: Evidence of Accelerated Englacial Warming in the Monte Rosa Area, Switzerland/Italy, The Cryosphere, 5, 231–243, https://doi.org/10.5194/tc-5-231-2011, 2011.

Hoffmann, H., Preunkert, S., Legrand, M., Leinfelder, D., Bohleber, P., Friedrich, R., and Wagenbach, D.: A New Sample Preparation System for Micro-[14]C Dating of Glacier Ice with a First Application to a High Alpine Ice Core from Colle Gnifetti (Switzerland), Radiocarbon, 60, 517–533, https://doi.org/10.1017/RDC.2017.99, 2018.

445   Holschuh, N., Christianson, K., and Anandakrishnan, S.: Power Loss in Dipping Internal Reflectors, Imaged Using Ice-Penetrating Radar, Ann. Glaciol., 55, 49–56, https://doi.org/10.3189/2014AoG67A005, 2014.

Holschuh, N., Parizek, B. R., Alley, R. B., and Anandakrishnan, S.: Decoding Ice Sheet Behavior Using Englacial Layer Slopes, Geophys. Res. Lett., 44, 5561–5570, https://doi.org/10.1002/2017GL073417, 2017.

Holschuh, N., Christianson, K., Paden, J., Alley, R., and Anandakrishnan, S.: Linking Postglacial Landscapes to Glacier Dynamics Using
450   Swath Radar at Thwaites Glacier, Antarctica, Geology, 48, 268–272, https://doi.org/10.1130/G46772.1, 2020.

Jenk, T. M., Szidat, S., Bolius, D., Sigl, M., Gäggeler, H. W., Wacker, L., Ruff, M., Barbante, C., Boutron, C. F., and Schwikowski, M.: A Novel Radiocarbon Dating Technique Applied to an Ice Core from the Alps Indicating Late Pleistocene Ages, JGR Atmospheres, 114, 2009JD011 860, https://doi.org/10.1029/2009JD011860, 2009.

Kapai, S., Schroeder, D., Broome, A., Young, T. J., and Stewart, C.: SAR Focusing of Mobile ApRES Surveys, in: IGARSS 2022 - 2022 IEEE
455   International Geoscience and Remote Sensing Symposium, pp. 1688–1691, IEEE, Kuala Lumpur, Malaysia, ISBN 978-1-66542-792-0, https://doi.org/10.1109/IGARSS46834.2022.9883784, 2022.

Koch, I., Drews, R., Franke, S., Jansen, D., Oraschewski, F. M., Muhle, L., Višnjević, V., Matsuoka, K., and Pattyn, F.: Radar Internal Reflection Horizons from Multisystem Data Reflect Ice Dynamic and Surface Accumulation History along the Princess Ragnhild Coast, Dronning Maud Land, East Antarctica, J. Glaciol., In press.

460   Konrad, H., Bohleber, P., Wagenbach, D., Vincent, C., and Eisen, O.: Determining the Age Distribution of Colle Gnifetti, Monte Rosa, Swiss Alps, by Combining Ice Cores, Ground-Penetrating Radar and a Simple Flow Model, J. Glaciol., 59, 179–189, https://doi.org/10.3189/2013JoG12J072, 2013.

Koutnik, M. R., Fudge, T. J., Conway, H., Waddington, E. D., Neumann, T. A., Cuffey, K. M., Buizert, C., and Taylor, K. C.: Holocene Accumulation and Ice Flow near the West Antarctic Ice Sheet Divide Ice Core Site, JGR Earth Surface, 121, 907–924,
465   https://doi.org/10.1002/2015JF003668, 2016.

Kusk, A. and Dall, J.: SAR Focusing of P-band Ice Sounding Data Using Back-Projection, in: 2010 IEEE International Geoscience and Remote Sensing Symposium, pp. 4071–4074, IEEE, Honolulu, HI, USA, ISBN 978-1-4244-9565-8, https://doi.org/10.1109/IGARSS.2010.5651038, 2010.

Licciulli, C., Bohleber, P., Lier, J., Gagliardini, O., Hoelzle, M., and Eisen, O.: A Full Stokes Ice-Flow Model to Assist the Inter-
470   pretation of Millennial-Scale Ice Cores at the High-Alpine Drilling Site Colle Gnifetti, Swiss/Italian Alps, J. Glaciol., 66, 35–48, https://doi.org/10.1017/jog.2019.82, 2020.

Lilien, D. A., Steinhage, D., Taylor, D., Parrenin, F., Ritz, C., Mulvaney, R., Martín, C., Yan, J.-B., O'Neill, C., Frezzotti, M., Miller, H., Gogineni, P., Dahl-Jensen, D., and Eisen, O.: Brief Communication: New Radar Constraints Support Presence of Ice Older than 1.5 Myr at Little Dome C, The Cryosphere, 15, 1881–1888, https://doi.org/10.5194/tc-15-1881-2021, 2021.

475 Looyenga, H.: Dielectric Constants of Heterogeneous Mixtures, Physica, 31, 401–406, https://doi.org/10.1016/0031-8914(65)90045-5, 1965.

Lüthi, M. and Funk, M.: Dating Ice Cores from a High Alpine Glacier with a Flow Model for Cold Firn, Ann. Glaciol., 31, 69–79, https://doi.org/10.3189/172756400781820381, 2000.

MacGregor, J. A., Fahnestock, M. A., Catania, G. A., Paden, J. D., Prasad Gogineni, S., Young, S. K., Rybarski, S. C., Mabrey, A. N., Wagman, B. M., and Morlighem, M.: Radiostratigraphy and Age Structure of the Greenland Ice Sheet, JGR Earth Surface, 120, 212–241,

480 https://doi.org/10.1002/2014JF003215, 2015.

Moran, M. L., Greenfield, R. J., Arcone, S. A., and Delaney, A. J.: Delineation of a Complexly Dipping Temperate Glacier Bed Using Short-Pulse Radar Arrays, J. Glaciol., 46, 274–286, https://doi.org/10.3189/172756500781832882, 2000.

NEEM community members: Eemian Interglacial Reconstructed from a Greenland Folded Ice Core, Nature, 493, 489–494, https://doi.org/10.1038/nature11789, 2013.

485 Nicholls, K. W., Corr, H. F., Stewart, C. L., Lok, L. B., Brennan, P. V., and Vaughan, D. G.: A Ground-Based Radar for Measuring Vertical Strain Rates and Time-Varying Basal Melt Rates in Ice Sheets and Shelves, J. Glaciol., 61, 1079–1087, https://doi.org/10.3189/2015JoG15J073, 2015.

Paden, J.: Synthetic Aperture Radar for Imaging the Basal Conditions of the Polar Ice Sheets, Ph.D. thesis, University of Kansas, https://web.archive.org/web/20170808175054id_/https://people.cresis.ku.edu/~paden/padenDissertation.pdf, 2006.

490 Peters, M., Blankenship, D., Carter, S., Kempf, S., Young, D., and Holt, J.: Along-Track Focusing of Airborne Radar Sounding Data from West Antarctica for Improving Basal Reflection Analysis and Layer Detection, IEEE Trans. Geosci. Remote Sensing, 45, 2725–2736, https://doi.org/10.1109/TGRS.2007.897416, 2007.

Peters, M. E., Blankenship, D. D., and Morse, D. L.: Analysis Techniques for Coherent Airborne Radar Sounding: Application to West Antarctic Ice Streams, JGR Solid Earth, 110, 2004JB003 222, https://doi.org/10.1029/2004JB003222, 2005.

495 Preunkert, S., Wagenbach, D., and Legrand, M.: A Seasonally Resolved Alpine Ice Core Record of Nitrate: Comparison with Anthropogenic Inventories and Estimation of Preindustrial Emissions of NO in Europe, JGR Atmospheres, 108, 2003JD003 475, https://doi.org/10.1029/2003JD003475, 2003.

Scanlan, K. M., Rutishauser, A., Young, D. A., and Blankenship, D. D.: Interferometric Discrimination of Cross-Track Bed Clutter in Ice-Penetrating Radar Sounding Data, Ann. Glaciol., 61, 68–73, https://doi.org/10.1017/aog.2020.20, 2020.

500 Schroeder, D. M., Castelletti, D., and Pena, I.: Revisting the Limits of Azimuth Processing Gain for Radar Sounding, in: IGARSS 2019 - 2019 IEEE International Geoscience and Remote Sensing Symposium, pp. 994–996, IEEE, Yokohama, Japan, ISBN 978-1-5386-9154-0, https://doi.org/10.1109/IGARSS.2019.8898737, 2019.

Schwikowski, B. M., Doscher, A., Gaggeler, H., and Schotterer, U.: Anthropogenic versus Natural Sources of Atmospheric Sulphate from an Alpine Ice Core, Tellus B, 51, 938–951, https://doi.org/10.1034/j.1600-0889.1999.t01-4-00006.x, 1999.

505 Shi, L., Allen, C. T., Ledford, J. R., Rodriguez-Morales, F., Blake, W. A., Panzer, B. G., Prokopiack, S. C., Leuschen, C. J., and Gogineni, S.: Multichannel Coherent Radar Depth Sounder for NASA Operation Ice Bridge, in: 2010 IEEE International Geoscience and Remote Sensing Symposium, pp. 1729–1732, IEEE, Honolulu, HI, USA, ISBN 978-1-4244-9565-8, https://doi.org/10.1109/IGARSS.2010.5649518, 2010.

Sigl, M., Abram, N. J., Gabrieli, J., Jenk, T. M., Osmont, D., and Schwikowski, M.: 19th Century Glacier Retreat in the Alps Preceded the
510   Emergence of Industrial Black Carbon Deposition on High-Alpine Glaciers, The Cryosphere, 12, 3311–3331, https://doi.org/10.5194/tc-
       12-3311-2018, 2018a.

Sigl, M., Abram, N. J., Gabrieli, J., Jenk, T. M., Osmont, D., and Schwikowski, M.: Black Carbon (rBC), Bismuth, Lead and Others from
       1741 to 2015 AD from Colle Gnifetti Ice Core (Swiss/Italian Alps), https://doi.org/10.1594/PANGAEA.894788, 2018b.

Vaňková, I., Cook, S., Winberry, J. P., Nicholls, K. W., and Galton-Fenzi, B. K.: Deriving Melt Rates at a Complex Ice Shelf Base Using in
515   Situ Radar: Application to Totten Ice Shelf, Geophys. Res. Lett., 48, e2021GL092 692, https://doi.org/10.1029/2021GL092692, 2021.

Wagenbach, D., Bohleber, P., and Preunkert, S.: Cold, Alpine Ice Bodies Revisited: What May We Learn from Their Impurity and Isotope
       Content?, Geografiska Annaler: Series A, Physical Geography, 94, 245–263, https://doi.org/10.1111/j.1468-0459.2012.00461.x, 2012.

Xu, B., Lang, S., Cui, X., Li, L., Liu, X., Guo, J., and Sun, B.: Focused Synthetic Aperture Radar Processing of Ice-Sounding Data Collected
       over East Antarctic Ice Sheet via Spatial-Correlation-Based Algorithm Using Fast Back Projection, IEEE Trans. Geosci. Remote Sensing,
520   60, 1–9, https://doi.org/10.1109/TGRS.2022.3198432, 2022.

Zeising, O., Steinhage, D., Nicholls, K. W., Corr, H. F. J., Stewart, C. L., and Humbert, A.: Basal Melt of the Southern Filchner Ice Shelf,
       Antarctica, The Cryosphere, 16, 1469–1482, https://doi.org/10.5194/tc-16-1469-2022, 2022.